EUROPEAN ORGANIZATION FOR NUCLEAR RESEARCH
European Laboratory for Particle Physics

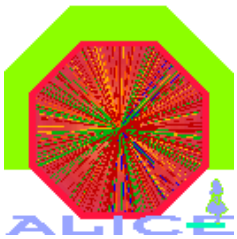

Dipartimento IA di Fisica
dell'Università and INFN

Bari, Italy

Internal Note/

ALICE reference number
ALICE-INT-2005-007 version 1.0
Institute reference number
[-]
Date of last change
November 26, 2004

Study of the ALICE Silicon Pixel Detector performance in a beam test at the SPS

Authors:

G.E. Bruno, M. Caselle, D. Elia[1], V. Manzari, F. Navach, R. Santoro

Abstract:

The performance of prototypes of the ALICE Silicon Pixel Detector has been studied during beam tests carried out in the last years at the CERN SPS. In this paper we report on recent results from the analysis of data collected in the 2003 test.
An assembly of the ALICE1 read-out chip with a 300 μm thick silicon sensor matrix has been placed in between two stations of tracking planes and exposed to the 120 GeV/c proton beam: results from a complete study of track impact reconstruction and detection efficiency as a function of the global threshold setting and of the track incidence angle are reported.

1Corresponding author, e-mail: Domenico.Elia@ba.infn.it

1 Introduction

The ALICE (A Large Ion Collider Experiment) detector has been designed to study strongly interacting matter created in the nucleus-nucleus collisions at LHC (Large Hadron Collider) [1]. The ITS (Inner Tracking System), placed close to the interaction point, is made of position sensitive detectors which will have to handle several thousands of particles per unit rapidity, produced at central rapidity. The two innermost layers will be equipped with ladders of Silicon Pixel Detector (SPD) placed at 3.9 cm and 7.6 cm from the beam line [2].
Spatial precision and hit efficiency of the SPD are crucial for ALICE, since the capability of the ITS to detect particles with open heavy-flavour [2, 3] will mainly depend on these parameters. In the 2003 test, a pixel chip has been exposed to a proton beam at the SPS, with four additional pixel planes used as tracking devices. The configuration of the tracking telescope and the cluster analysis of the hits allowed us to study in detail the intrinsic spatial precision of the plane under test and its detection efficiency. Moreover, we have found that the frequency of different cluster topologies highly depends on threshold settings and particle incident angle on the detector: this is mainly due to the influence of these parameters on the spread of the generated charge among neighbouring pixels. In the present paper the behaviours of the detector spatial precision and efficiency under different conditions are discussed.

2 The ALICE pixel detector and the 2003 beam test

The basic detector unit of the ALICE SPD is the ladder. A ladder is a silicon two-dimensional matrix of p^+n reversed bias diodes flip-chip bonded to five readout chips. Each individual cell of the detector matrix is connected via a Sn-Pb solder bump of $\approx$ 25 μm diameter to a front end chip cell of the same size, containing the front-end readout electronics. The size of the individual pixel cell is 50 x 425 μm^2.
To fulfil the total material budget allowed for the SPD, in the final configuration the sensor substrate will be 200 μm thick and the front-end chip substrate will be thinned down to 150 μm from the native 750 μm. The readout chip (ALICE1) is a mixed analog-digital signal ASIC built using a 6-metal-layer commercial 0.25 μm CMOS technology which have been made radiation tolerant by the layout design [4].
A test phase has been carried out in October 2003 on the H4 beam line at the CERN SPS, by using both 120 GeV/c protons and 158 A GeV/c indium ions [5]. Different configurations have been implemented during the test, mainly changing the de-

tectors and/or their position in the layout: the analysis described in the following is based on the data collected with protons in the configuration schematically shown in Fig.1. The first and the last pair of detectors, called *minibus 0* and *minibus 1*, were used as tracking telescope: in each of the two pairs the detectors were arranged in crossed geometry in order to optimize the measurement of the transverse position of the incident beam particles in both x and y coordinates. The detector under test was a prototype of the ALICE SPD made by an assembly of a 300 μm thick sensor and 750 μm thick ALICE1 front-end chip. It was placed in between the two minibuses, each made of thiner assemblies of the same front-end chip and 200 μm thick sensor. The transverse position and the tilt angle of the test plane with respect to the beam line could be changed by a remote controlled stepping motor. The trigger signal was set by an incoming beam particle passing through scintillator counters.

Data has been collected with different inclination angles of the normal to the test plane with respect to the beam line (0, 10, 20, 30, 40 and 45 degrees) along an axis parallel to the 425 μm cell size direction (x coordinate): for each inclination angle a full scan of the global threshold setting on the detector has been performed, namely in DAC units from 214 (corresponding to about 2000 electrons) down to 0. Each 15 units decrease in DAC value corresponds to about 1000 electrons increase in the effective global threshold: this linearity holds for DAC values above 150. For details on the measurement of mean threshold and mean noise as a function of the global threshold setting on the chip see [6]. Data with large statistics taken with beam focussed on the center of the detector areas has been used for studies on the precision in reconstructing the track impact position, while checks of the detector efficiency uniformity over the full plane have been based on the analysis of lower statistics samples taken with wide beam configuration.

3 Data analysis and results

The analysis of data with focussed beam at normal incident angle with respect to the pixel planes and typical operating threshold of 200 DAC units (corresponding to about 3000 electrons) is first discussed. Fig.2 shows an example of a raw hit maps for this data. In the following subsections the cluster analysis and the alignment procedure will be described. Tracks reconstructed by using the minibus planes have been used to estimate the detector efficiency which has been then studied as a function of the threshold setting. The estimate of the tracking error and the study of the distribution of track impact residuals on the test plane allow us to extract the intrinsic spatial precision of the detector.

3.1 Cluster analysis

As a preliminary step, the hits on each plane are processed by a cluster finder algorithm, where a cluster is by definition either a single fired pixel or a group of fired pixels, each of them being adjacent to at least another one. For each event and each plane, the cluster finder analysis works out the number of clusters and, for each cluster, the number of hit pixels (cluster size), the x and y dimensions and the topology. Fig.3 illustrates the cluster topology numbering conventionally used in the present study.

Events are first selected by requiring one and only one cluster on each of the tracking planes, with maximum cluster size 2: with this condition we avoid more complicated cluster topologies corresponding to worse estimations of the track impact points on those planes. As shown in Fig.4 (left side) most of the clusters fulfil this requirement; $dimx$ and $dimy$ variables on the right hand side plot of the same figure correspond to the dimensions of the minimal area box containing the cluster. Due to the shorter pixel size in the y coordinate for plane 1, the cluster is in average much more developped in this direction.

As discussed in the following, once planes are aligned we make a best fit to reconstruct the beam track by using the minibus doublets and then we apply a second event selection by requiring that the beam passes through the sensitive area of the detector under test. We define a cluster on the test plane to be correlated to the beam track when the residual between track prediction from the telescope (interpolated impact) and the mean cluster position is below a defined maximum distance (namely $\Delta x < 600$ μm and $\Delta y < 150$ μm). In Fig.5 the frequency of each topology for clusters on the test plane, for 200 DAC units threshold, is shown: only clusters correlated to the traversing track are taken into account. In these conditions most of the clusters are just single (58%) or double pixel along y (35%) ones, while topologies 6, 11, 12 and 13 (more developped along the 425 μm cell size dimension) are missed. This pattern rapidly changes with threshold setting and track incidence angle on the detector, since most of it is determined by charge sharing and geometrical effects: the corresponding behaviours will be discussed in the following of the paper.

3.2 Alignment procedure and tracking error estimation

Before starting the track reconstruction procedure, the relative misalignments of the detectors in the transverse directions has to be taken into account. As a first step, an internal alignment for each of the two minibuses has been achieved by using the correlations of the cluster positions on each of the two component detectors. We use kind of plots like

those in Fig.6, where the correlations between cluster coordinates in the first minibus, before the alignment corrections, are shown. The procedure assumes that clusters on the planes are only due to the beam track (no noisy hits) and that the track itself crosses the detectors at normal incidence: both assumptions are very reasonable in this case.
The next step is to produce the relative alignment of the two minibuses. This is again achieved by cluster coordinate correlations: for a given cluster on each minibus, we take the x coordinate from the second plane and the y coordinate from the first plane so to use the best measurements in both directions thanks to the crossed geometry.
Once tracking planes are preliminarly aligned, a least squares fit procedure is applied to reconstruct the beam track both in the xz and yz projections. The residual distributions on the test planes (difference between predicted impact and nearest cluster positions) can be calculated: centering these distributions provides the alignment of the test plane. This procedure allowed us also to correct for a rotation of the test detector (by $\approx 12\ mrad$) in the transverse plane. With an iterative procedure, which escludes one plane at a time from the fit, we were able to fine tune the alignment constants also for the tracking detectors. Of course, the alignment of the test plane needed to be re-calculated for each of the data sets of this configuration, whenever the transverse coordinates or the inclination angle of the plane were changed. As an example of the data sample quality, we report in Fig.7 the χ^2 distributions from the track fits in both projection planes once all the tracking detectors have been aligned.
To calculate the intrinsic precision of the test plane from the track impact residuals, an estimation of the tracking errors is required. A simulation taking into account the telescope geometry, multiple scattering and residual plane misalignments effects has been developped. Details on the amount of material budget to take into account for multiple scattering can be found in [7]. A track is propagated through the telescope, its impacts on each plane generate a digit (hit pixel) and the four digits are then used to fit a "reconstructed" track: the distribution of the differences between the predicted impact and the crossing point of the generated track on test plane gives the tracking precision. Since one of the inputs of the simulation (the errors for the points on the tracking planes) is based on the intrinsic precision itself, an iterative procedure has to be applied: we stop the iteration when the difference between the input intrinsic precision and the intrinsic precision as calculated from residuals (by using the current tracking precision estimation) gets below a given tolerance which has been set to 0.1 μm.
The described procedure gives an estimate of the precision in the track impact prediction on the test plane as provided by the telescope. Residuals distributions in Fig.8 show that it corresponds to $\sigma_{track} \approx 10\ \mu m$ in both transverse coordinates.

3.3 Track impact residuals and detector spatial precision

Fig.9 illustrates, from top to bottom, the position of the predicted impact scaled to a single pixel cell reference system, in the cases of single (topology 1), double-x (topology 3) and double-y (topology 2) pixel clusters. As expected, when a single pixel responds to the incident particle, most of the hits are located in a region well inside the cell area, while in case two pixels are fired the impact points are mainly concentrated on the pixel borders. The width of the border region depends on the threshold setting and, of course, on the precision of the impact prediction. The projections of the impacts along x coordinate for topologies 1 and 3 are shown in Fig.10: when a single pixel is fired then the track has crossed the pixel itself, with roughtly uniform probability along x, in a region slightly smaller then the pixel size in the same direction (a similar effect is present also in the other coordinate). This clearly has an effect on the track impact precision, as discussed hereafter.

The spatial precision of the detector, in absence of the analog information about the collected charge in each sensor cell, is basically determined by the cell size and by some degree of charge sharing between neighbouring cells. Neglecting this last factor, the theoretical value for the spatial precision in the x coordinate is given by:

$$\sigma^{th}_{pixel}(x) = L_x/\sqrt{12} \tag{1}$$

and by a similar expression for the y coordinate, where L_x and L_y are the different sizes of the detection element along the two orthogonal measuring directions. By applying expression (1) to the ALICE pixel detector, with $L_x = 425\ \mu m$ ("column direction") and $L_y = 50\ \mu m$ ("row direction"), we obtain:

$$\sigma^{th}_{pixel}(x) = 122.7\ \mu m \qquad \sigma^{th}_{pixel}(y) = 14.4\ \mu m \quad . \tag{2}$$

Fig.11 shows the total residual distribution, while Fig.12 and Fig.13 show the two cases of single pixel clusters and double ones, respectively. In particular, for Fig.13 the x-residual distribution is based on class 3 cluster topology while the y-residuals are calculated for class 2 topologies only. As expected, since the single pixel clusters on the test plane are generated by track impacts located in a narrower region than $L_x \cdot L_y$, the corresponding residual distribution also becomes narrower. All the distributions have been obtained by reconstructing tracks in events with single clusters (by one or two pixels) on each of the tracking planes, as mentioned in section 3.1.

To disentangle the intrinsic spatial precision of the detector from the widths of the mea-

sured residual distribution we have taken into account the telescope tracking precision. As an approximation (see also [7]) we have assumed the following expression:

$$\sigma^2_{pixel}(x) = \sigma^2_{resid}(x) - \sigma^2_{track} \tag{3}$$

and a similar one for the y coordinate, where $\sigma_{resid}(x)$ and $\sigma_{resid}(y)$ are the sigmas of the gaussian fits to the measured x and y-residual distributions respectively, while σ_{track} is about 10 μm in both coordinates, as already mentioned in section 3.2.
As shown in Fig.12, for single-pixel clusters the x-residual distribution is much wider and approximately flat: in this case as $\sigma_{resid}(x)$ we use the rms of the distribution. In this way, the intrinsic precisions for single-pixel clusters are found to be:

$$\sigma^{cls1}_{pixel}(x) = (\ 120.1 \pm 0.5\ )\ \mu m \qquad \sigma^{cls1}_{pixel}(y) = (\ 11.0 \pm 0.5\ )\ \mu m \quad . \tag{4}$$

Of course, a particle crossing the detector within a small region from the border (charge sharing region) may generate two-pixel clusters with much improved precision in the impact localization. This explain the narrower double-pixel cluster residual distributions shown in Fig.13, from which we obtain:

$$\sigma^{cls2}_{pixel}(x) = (\ 7.7\ \pm\ 0.9\ )\ \mu m \qquad \sigma^{cls2}_{pixel}(y) = (\ 9.2\ \pm\ 0.6\ )\ \mu m \quad . \tag{5}$$

Errors on the estimates of the intrinsic precision have been calculated by taking into account both the contributions due to uncertainties in σ_{resid} and σ_{track}. Comparable results have been also obtained with a different approach [7].
There are many factors influencing the cluster topology distribution (e.g. inter pixel capacitance, pixel capacitance to backplane, readout electronics crosstalk, etc) but it is mainly determined by the charge sharing effect. Different behaviours observed by varying the global threshold setting and the particle incidence angle on the detector will be discussed in sections 4 and 5.

3.4 Detector efficiency

As already anticipated, it was required for the selected events that the reconstructed beam track (obtained by fitting the four telescope points) had a predicted impact on the test plane falling in a fiducial region slightly smaller than the detector sensitive area. This last requirement was applied to make sure that edge effects due to relative misalignments of the planes do not bias the detector efficiency estimate.

The efficiency of the test plane has been defined as the ratio between the number of events where a cluster correlated to a reconstructed track (see definition in section 3.1) is detected and the total number of events with a reconstructed track crossing the test plane in the fiducial region mentioned above. The efficiency calculation has been based on large number of tracks ($\sim$ 20,000) and cross checked for uniformity all over the detector active area. For threshold value at 200 DAC units and normal track incidence angle the efficiency has been found to be larger than 99%.

4 Study of global threshold scan

All the studies illustrated in the previous sections have been carried out also as a function of the global threshold setting on the detector readout. The cluster distributions, with corresponding boundary box dimensions, are shown in Fig.14 for threshold values of 214, 210, 200 and 150 DAC units, from left to right respectively.

The increase of average cluster size as a function of a decreasing threshold setting is shown in Fig.15. At very high thresholds (below 100 DAC units) the average cluster size gets stabilized at the minimum value of 1, even if the detection efficiency for those settings is very low: it simply reflects the event selection which takes into account only events with a correlated cluster on the test plane. The increase with respect to the minimum begins to take place around thresholds of 80-100 DAC units.

A detailed study of the cluster shapes has also been carried out by looking at the cluster topology distributions for different threshold settings: as an example in Fig.16 we report those corresponding to thresholds 214, 210 (top left and right), 180 and 140 (bottom left and right) DAC units, to be compared with that at 200 DAC units already shown in Fig.5. The study of the detector behaviour as a function of the cluster shape as well as the study as a function of the track incidence angle, which is discussed in the next section, is very useful for the fine tuning of the detector response function in the simulation model [8].

The spatial precision of the detector has been studied as a function of the threshold. Results are reported in Fig.17 where residuals and intrinsic precisions in the 50 μm pixel size coordinate are shown. In the plots the precision estimates corresponding to single and double-y pixel clusters have been shown separately. We see that for single pixel clusters at high thresholds (e.g. 150 DAC units) the intrinsic precision goes close to $L_y/\sqrt{12}$, as expected. For decreasing threshold (increasing DAC values) it decreases: this reflects the fact that, lowering the threshold, tracks impacting the cell close enough to boundary regions can fire a double pixel cluster.

Of course, the width of this boundary region, which we can call as "region useful for double

pixel cluster", increases for decreasing thresholds: at about 210 DAC units it reaches its maximum and the same amount of single and double-y pixel clusters occur (see Fig.14 and Fig.16). In these conditions the intrinsic precision is about the same for both topologies (single and double pixel clusters) and the global precision of the detector reaches its best value. The curve for double pixel clusters in the same Fig.17 correspondigly increases with decreasing thresholds, at least for DAC values larger that 170. Below 170 DAC units cluster topologies that would have been made by 3 or 4 pixels for softer threshold values come in the double-y pixel cluster sample, then making the corresponding average precision slightly worse. For completeness in Fig.18 we report the corresponding behaviour of the intrinsic precision along the large pixel size coordinate, for both single and double-x pixel clusters.

The detection efficiency has also been studied as a function of the threshold: Fig.19 shows the wide plateau at values larger than 99%, starting from threshold settings well above the usual operating range of the detector.

5 Study of track inclination angle scan

The dependence of the detector performance as a function of the angle of incidence of the beam track with respect to the normal to sensor surface has been studied. As already mentioned, data samples at 0, 10, 20, 30, 40 and 45 degrees were taken with different threshold settings.

Fig.20 schematically illustrates the maximum number of pixel cells traversed by a track at three different incidence angles. Simple geometry basically explains the evolution of the cluster sizes at different incidence angles, shown in Fig.21 as a function of the readout threshold. The threshold value where the curve starts increasing with respect to the miminum clearly depends on the track incident angle: for larger angles a lower threshold is required to let the traversed cells to respond. It is also interesting to plot the average cluster size as a function of the track incidence angle for some of the threshold settings: the result is reported in Fig.22 for thresholds corresponding to 214, 200, 170 and 160 DAC units. As already observed in previuos studies [9], for very hard thresholds the average cluster size at large angle decreases due to the decreasing charge deposition per cell when many cells are traversed. In usual operating conditions (thresholds at 200 or 214 DAC units) at large angles the cluster size is compatible with the firing of 6-7 cells as expected by the geometry. The change in the cluster topology is shown in Fig.23 for 0 and 20 degrees incident angles.

Fig.24 shows the efficiency curves as a function of the threshold at three different angles.

Also for very large incidence angles the detector has full efficiency with a large plateau including the usual operating range. As expected, the full efficiency region starts at lower thresholds as far as the incidence angle increases.
Finally, the study of the spatial precision for the y coordinate as a function of the DAC settings for different track incidence angles is shown in Fig.25. In the top we report the sigmas of the gaussian fits to the corresponding residual distributions at all the considered incidence angles: it clearly appears that for increasing threshold (decreasing DAC units value) the precision for 45 degrees incident tracks becomes much worse. This can be explained taking into account that for such large angles many pixel cells are traversed and the harder the thresholds the fewer of them are fired, so producing an increasing uncertainty on the cluster prediction for the track impact.
A detail in expanded scale (only for 0, 10 and 20 degrees incident tracks) is shown in the middle plot of the same Fig.25. For each angle, the best precision is achieved at some defined threshold value. For instance, at 20 degrees the best value is around 185 DAC units threshold: for harder threshold less pixels are fired so giving a poorer information, while for softer thresholds also cells with a small traversing path of the track inside them are fired, so spoiling the impact prediction. The plot on the bottom of Fig.25 finally shows the same behaviour for the intrinsic y-precision, i.e. after subtracting the telescope tracking error contribution. Like for normal incidence tracks, also for 10 and 20 degrees inclination angle tracks the optimal condition for the spatial precision is achieved when the main cluster topologies occur with equal frequency: this is shown in Fig.26 and Fig.27.

6 Summary

A study of the ALICE Silicon Pixel Detector performance using data collected in the 2003 beam test at the SPS has been described. The detection efficiency and the intrinsic precision in reconstructing track impact position have been studied as a function of both threshold setting and track incident angle. Results confirm the very high efficiency ($>$ 99%) of the detector in a wide range containing the typical operating point and an intrinsic spatial precision below 10 μm in the 50 μm cell size coordinate.

References

[1] ALICE Collaboration, *Technical Proposal*, CERN/LHCC 95-71.

[2] ITS Technical Design Report, CERN/LHCC 99-12, 1999.

[3] F. Antinori *et al.*, ALICE Internal Note, ALICE-INT-2004-12.

[4] R. Dinapoli *et al.*, Proceedings of the 6^{th} Workshop on Electronics for LHC Experiments, Krakow (Poland), September 2000, CERN-2000-010.

[5] P. Nilsson *et al.*, Proceedings of the 10^{th} Vienna Conference on Instrumentation, Vienna (Austria), February 2004, to be published on NIM A.

[6] P. Riedler *et al.*, Proceedings of the 10^{th} International Workshop on Vertex Detectors, Brunnen (Switzerland), September 2001, Nucl. Instrum. Methods Phys. Res. A501 (2003), 111-118.

[7] J. Conrad and P. Nilsson, *"Techniques to estimate the intrinsic resolution of the ALICE Silicon Pixel Detector"*, to be published as an ALICE Internal Note.

[8] R. Caliandro *et al.*, ALICE Internal Note, ALICE-INT-2000-23.

[9] J.J. van Hunen *et al.*, Proceedings of the 7^{th} Workshop on Electronics for LHC Experiments, Stockholm (Sweden), September 2001, CERN-2001-005.

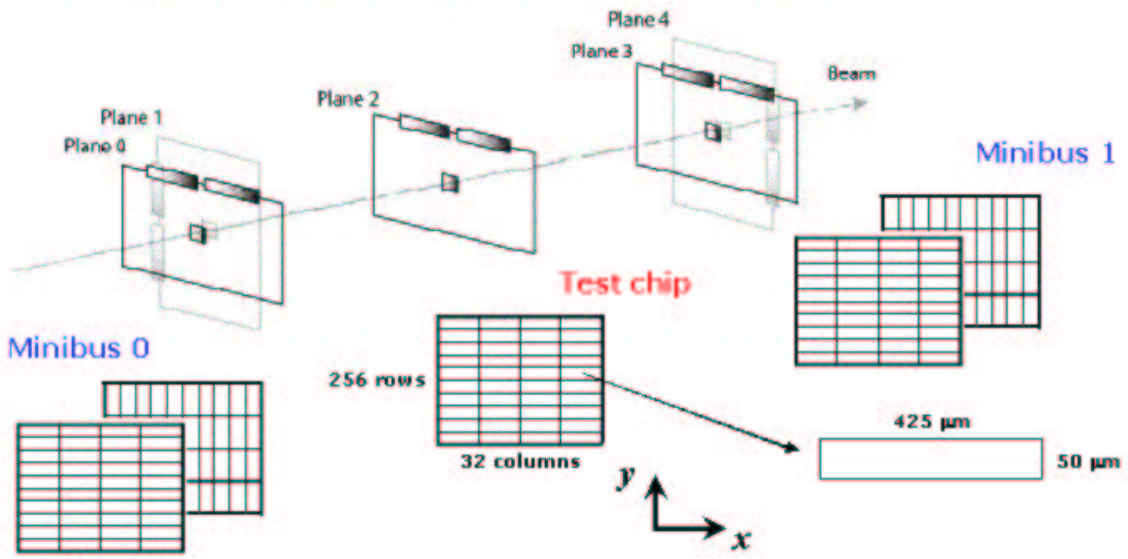

Figure 1: Schematic view of the test layout for the proton beam data taking.

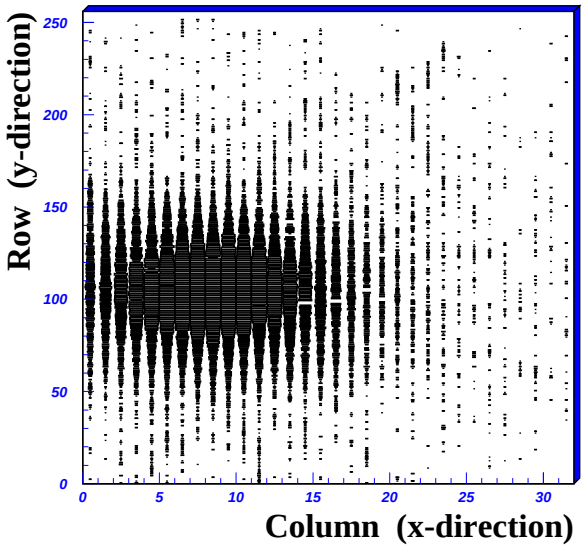

Figure 2: Raw hit map for data with focussed beam.

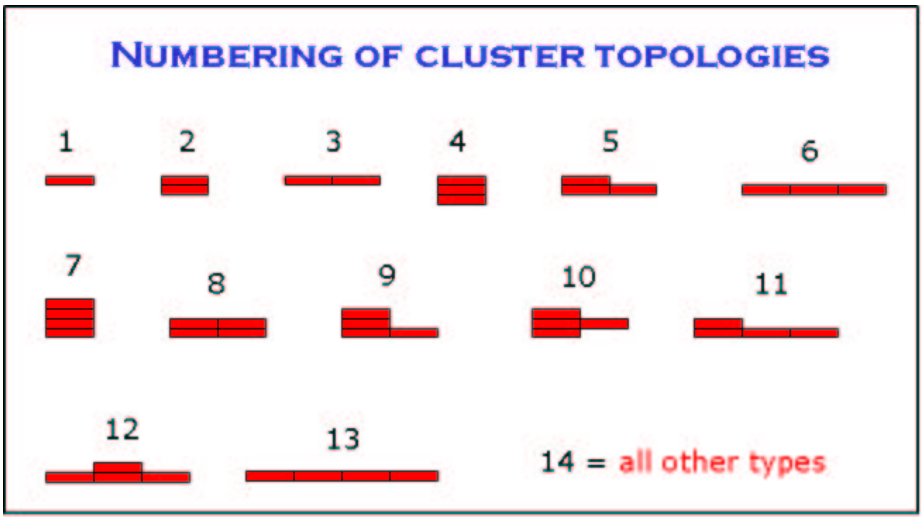

Figure 3: Numbering of the main pixel cluster topologies.

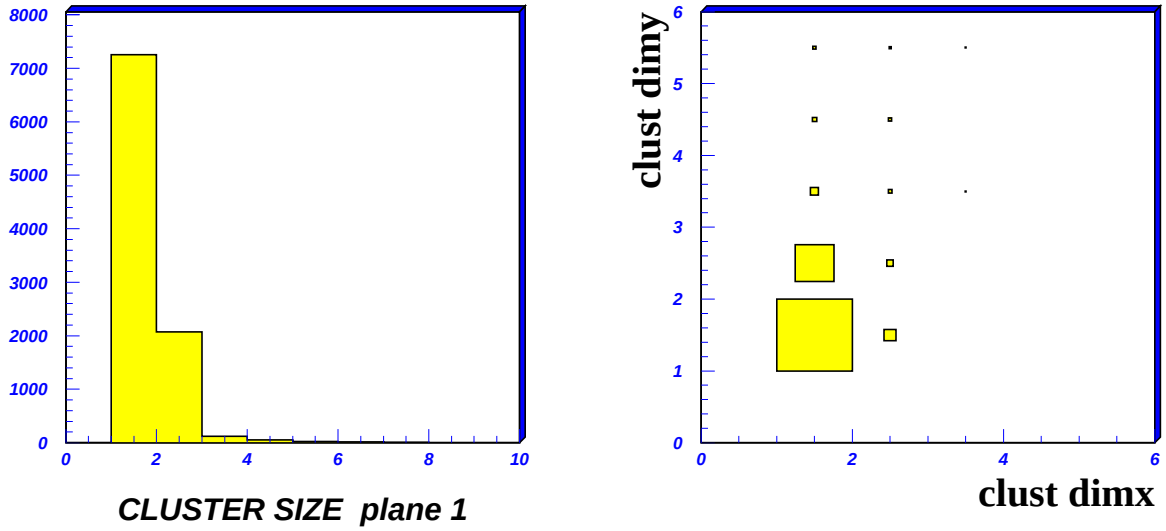

Figure 4: Cluster size distribution (left) and cluster containing box dimensions (right) for the first tracking telescope plane.

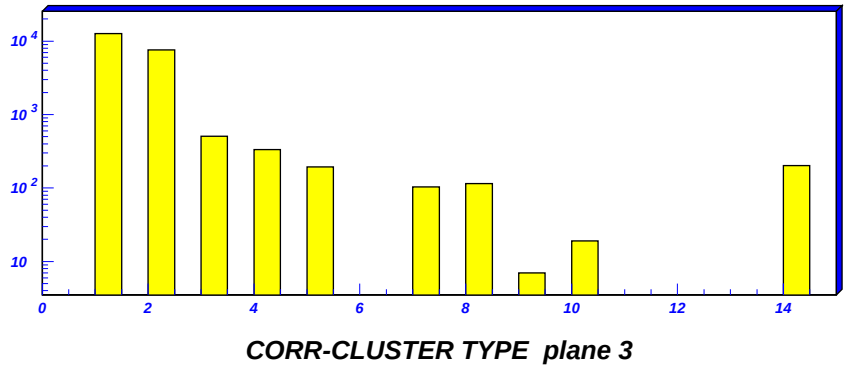

Figure 5: Distribution of cluster topologies on the test plane, for normal incidence tracks and threshold setting 200 DAC units.

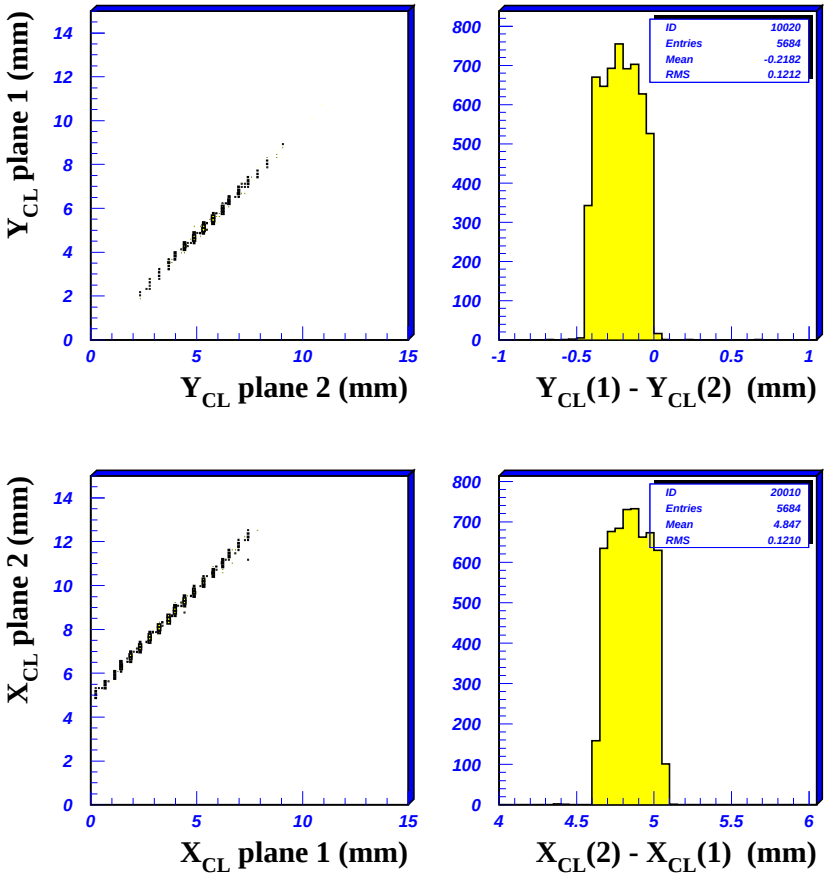

Figure 6: Correlation between cluster position coordinates for the planes in the first minibus (left) and corresponding cluster position difference distributions (right).

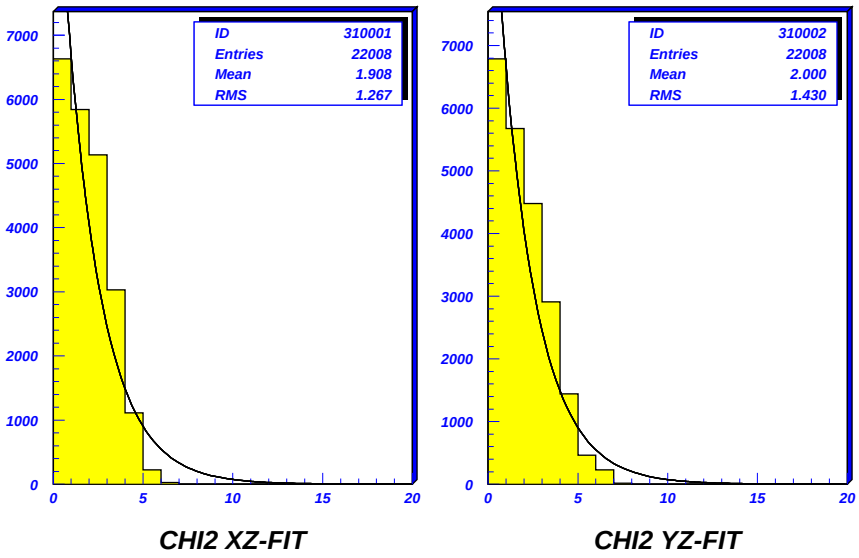

Figure 7: χ^2 distributions from track fits in the xz and yz projection planes. Superimposed curves correspond to the theoretical χ^2 distributions for two degrees of freedom.

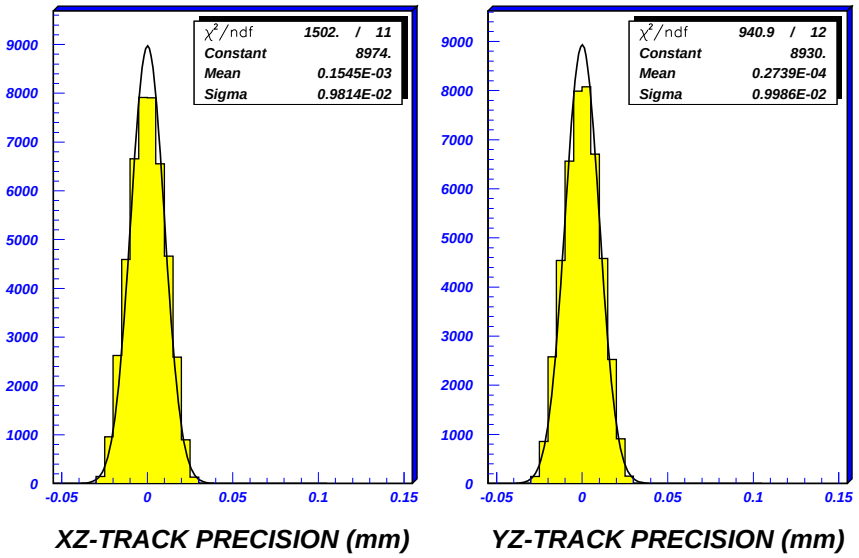

Figure 8: Difference between predicted impacts and track crossing point from geometrical simulation, in both transverse coordinates.

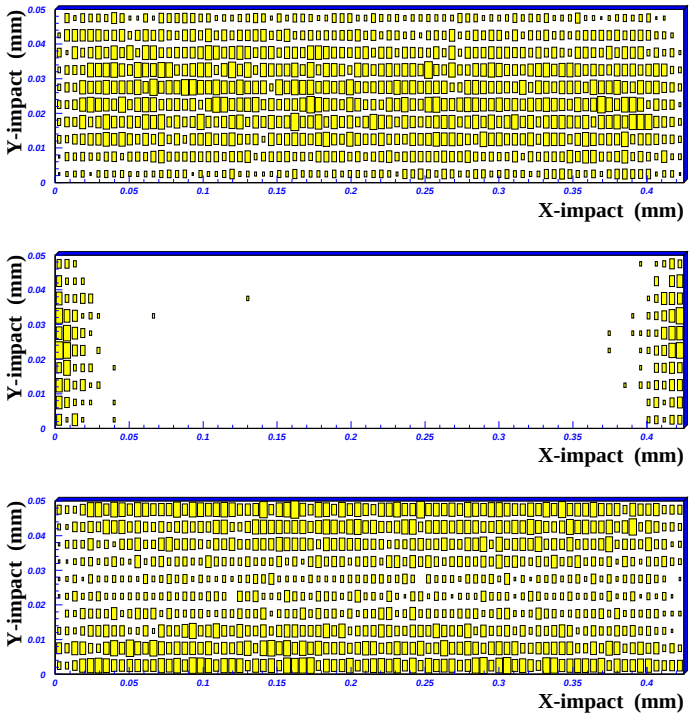

Figure 9: Impact points on the test plane, scaled to a single pixel cell, as predicted from the telescope: from top to bottom plots correspond to cluster topologies 1, 3 and 2 respectively. Data corresponds to normal track incidence and 200 DAC units threshold.

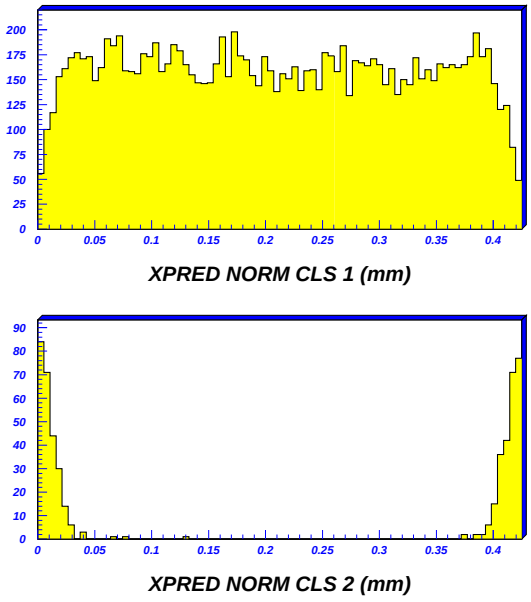

Figure 10: Projections along x coordinate of the impact points on the test plane for cluster topologies 1 (top) and 3 (bottom).

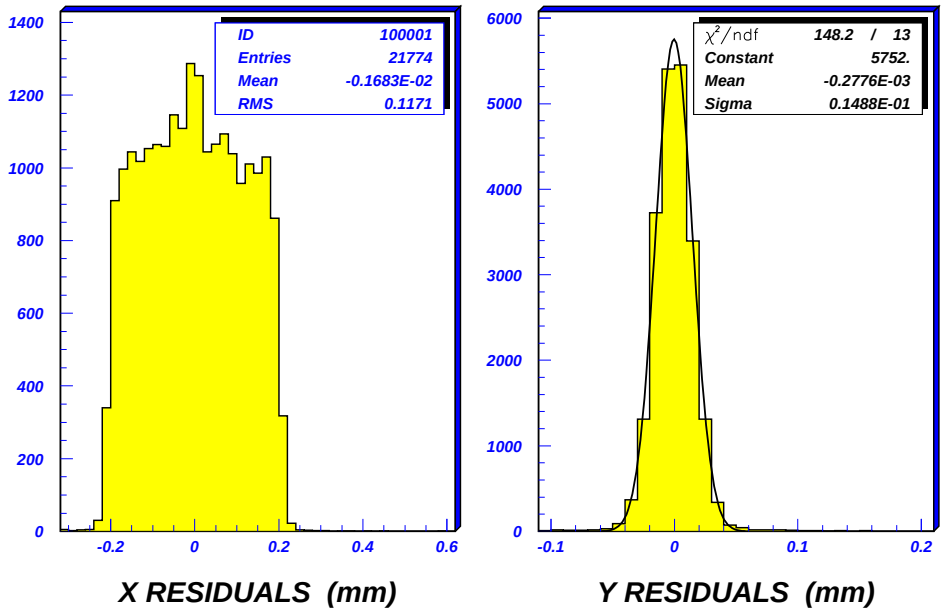

Figure 11: Residuals between predicted impact from the telescope and that from clusters on the test plane.

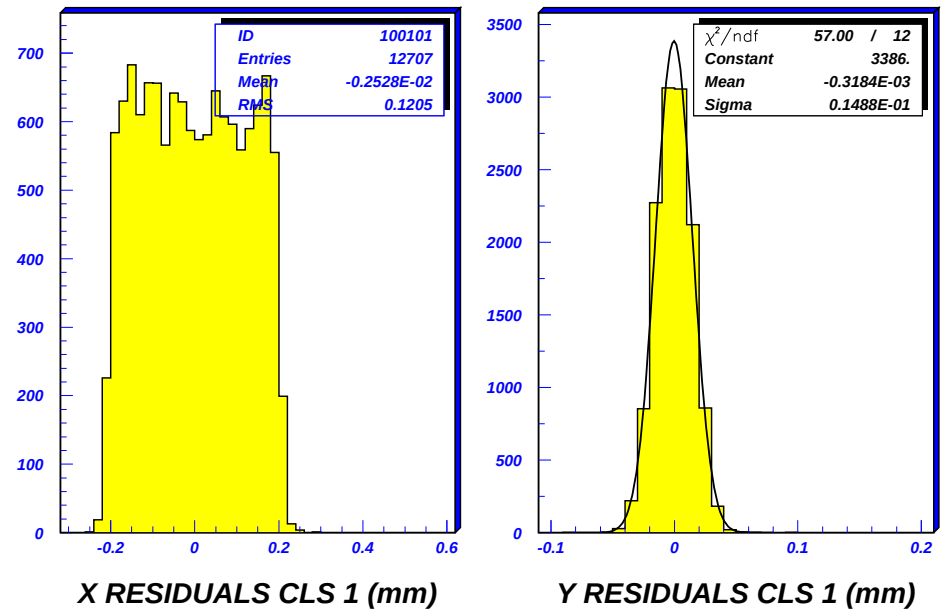

Figure 12: Residuals distributions for single pixel clusters.

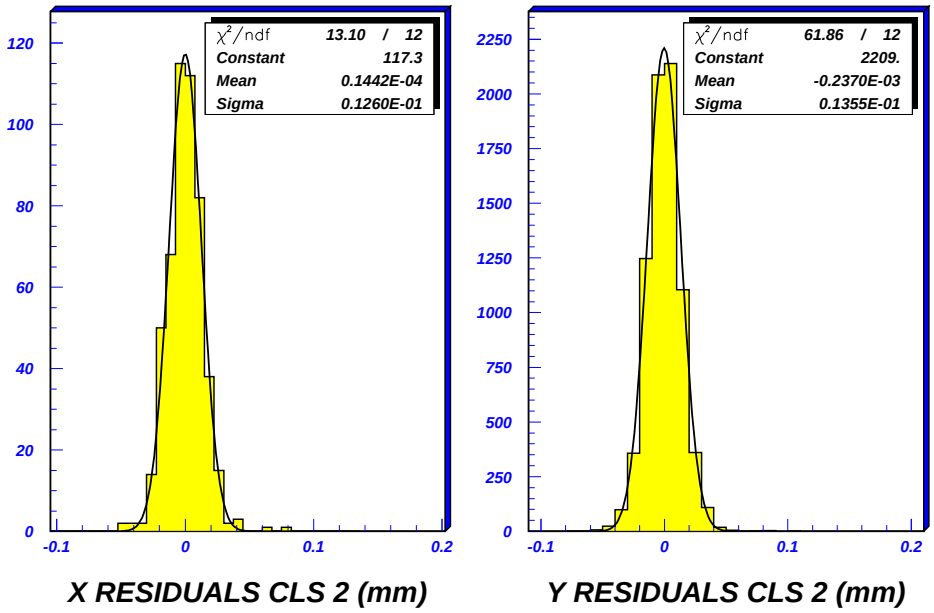

Figure 13: Residuals distributions for double pixel clusters, for topology 3 (left) and topology 2 (right) only.

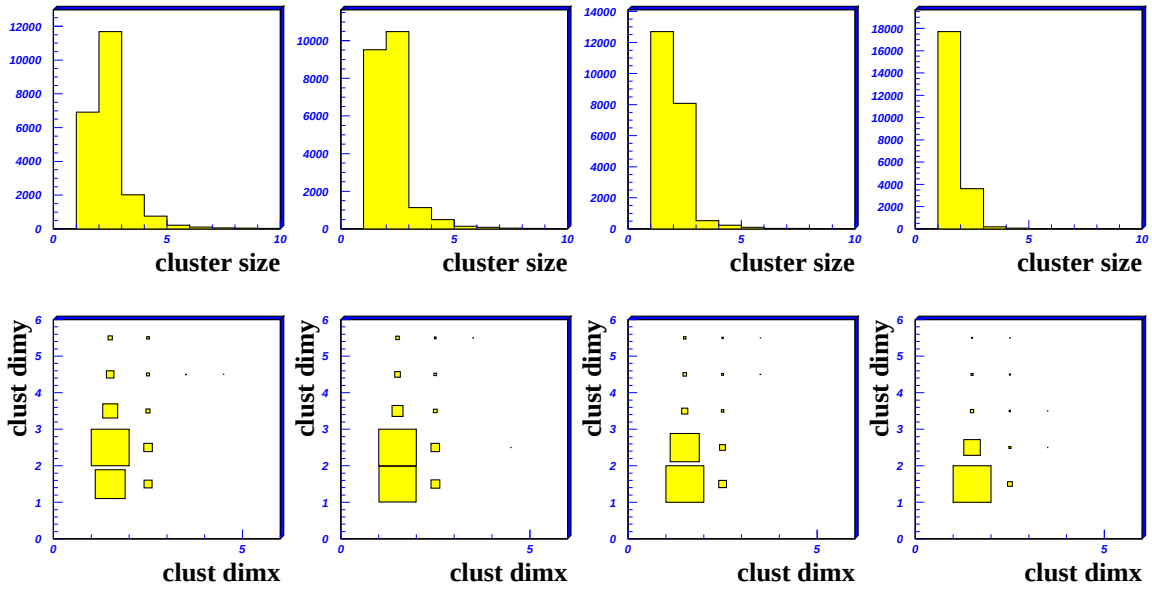

Figure 14: Cluster distributions: from left to right threshold settings correspond to 214, 210, 200 and 150 DAC units.

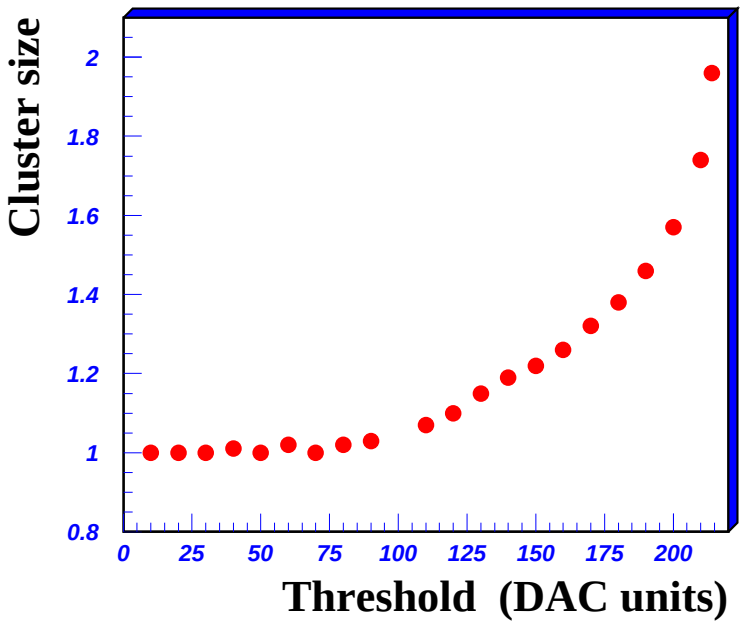

Figure 15: Average cluster size as a function of the threshold setting for normal track incidence angle.

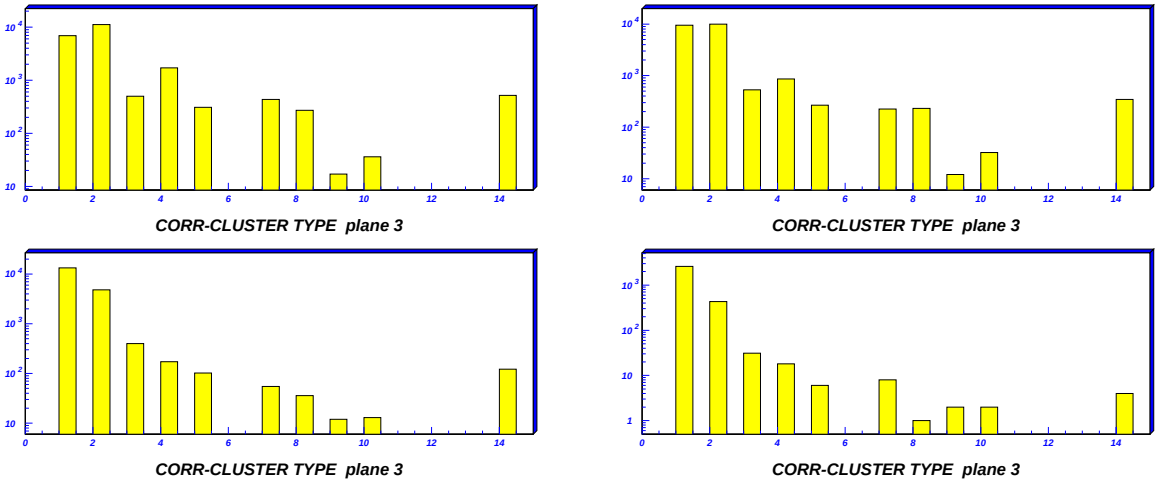

Figure 16: Cluster topology distributions for threshold settings of 214, 210 (top left and right), 180, 140 (bottom left and right) DAC units.

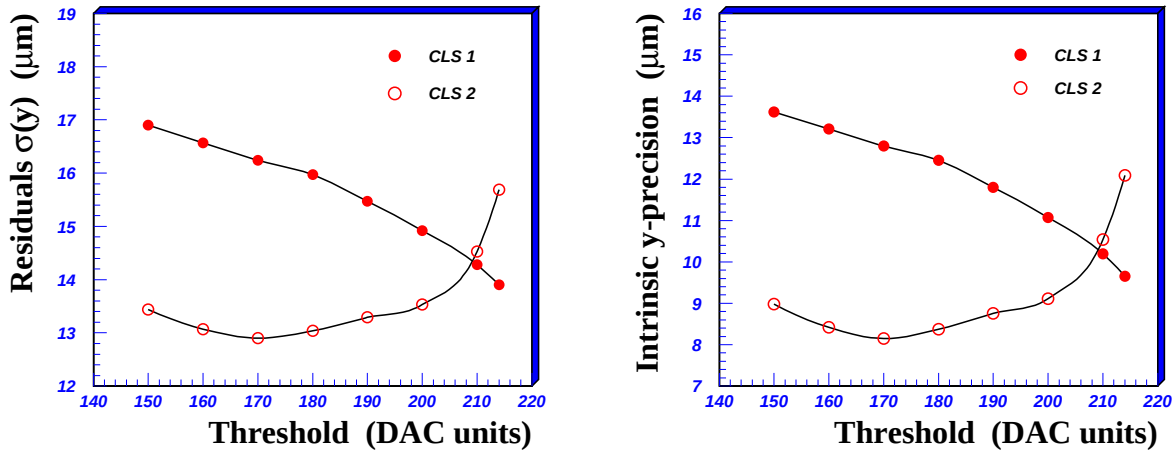

Figure 17: Width of the residual distribution along y coordinate as a function of the threshold (left) and corresponding intrinsic precision after subtraction of the telescope prediction uncertainty (right), for normal track incident angle samples.

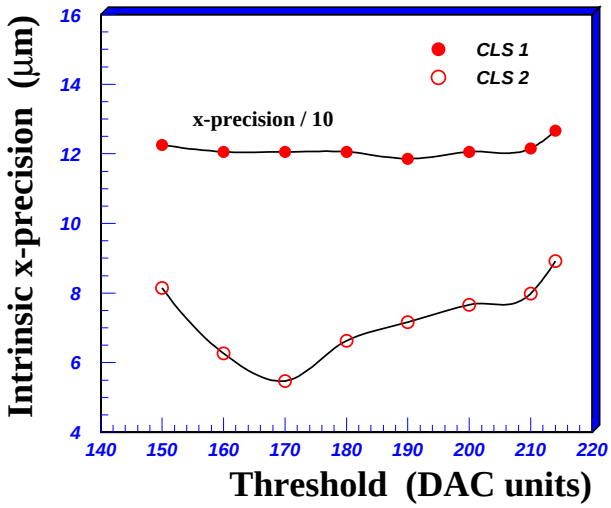

Figure 18: Intrinsic precision along the x coordinate for normal track incident angle samples: for single pixel clusters the precision has been scaled by a factor 10 in the picture.

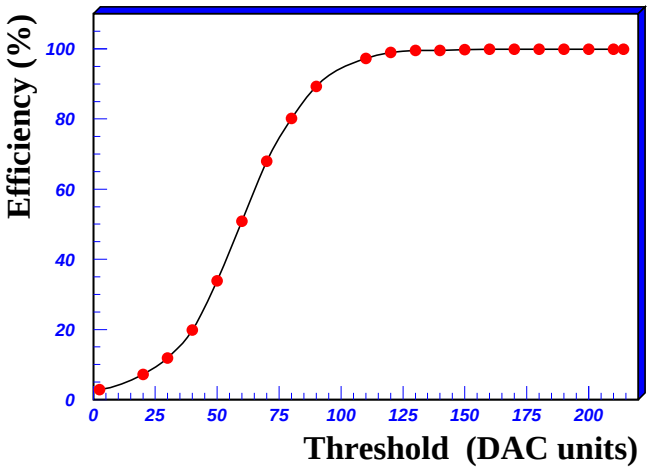

Figure 19: Detection efficiency as a function of the threshold for normal track incidence angle.

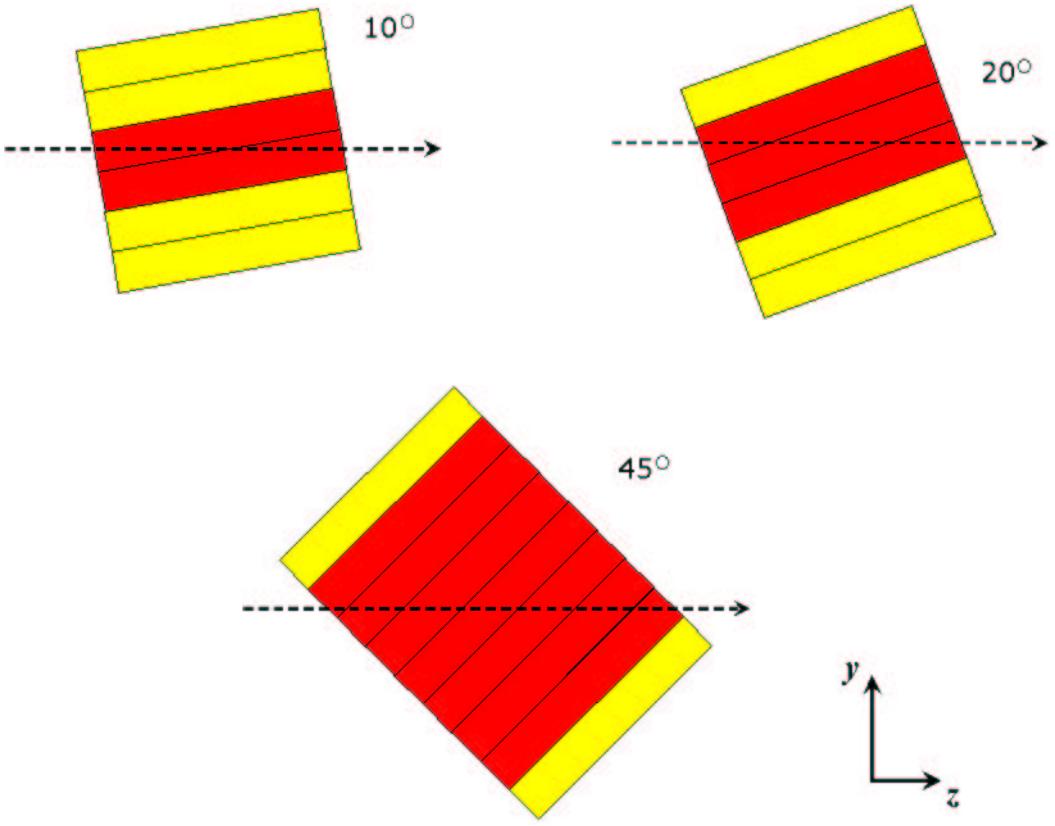

Figure 20: Schematic pictures of pixel planes crossed by tracks at different angles. Pixel cells traversed by the track are shown in red.

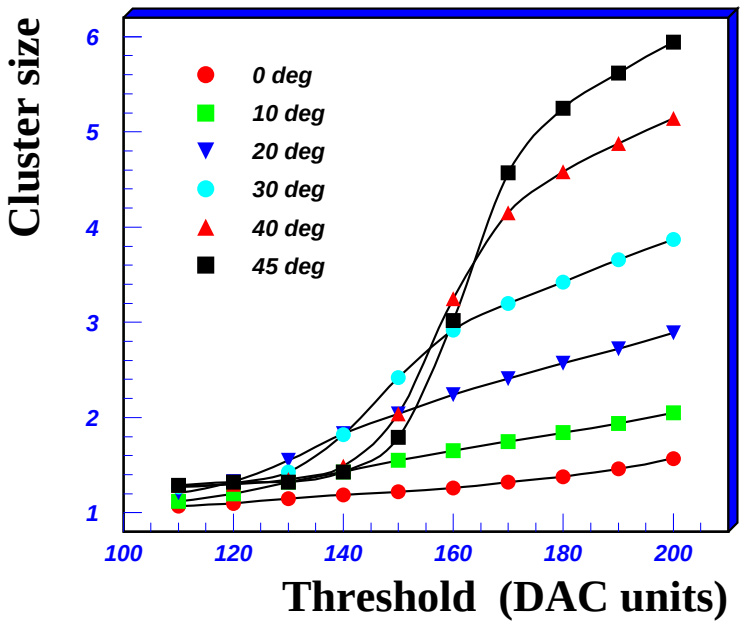

Figure 21: Average cluster size as a function of the threshold setting for different track incidence angles.

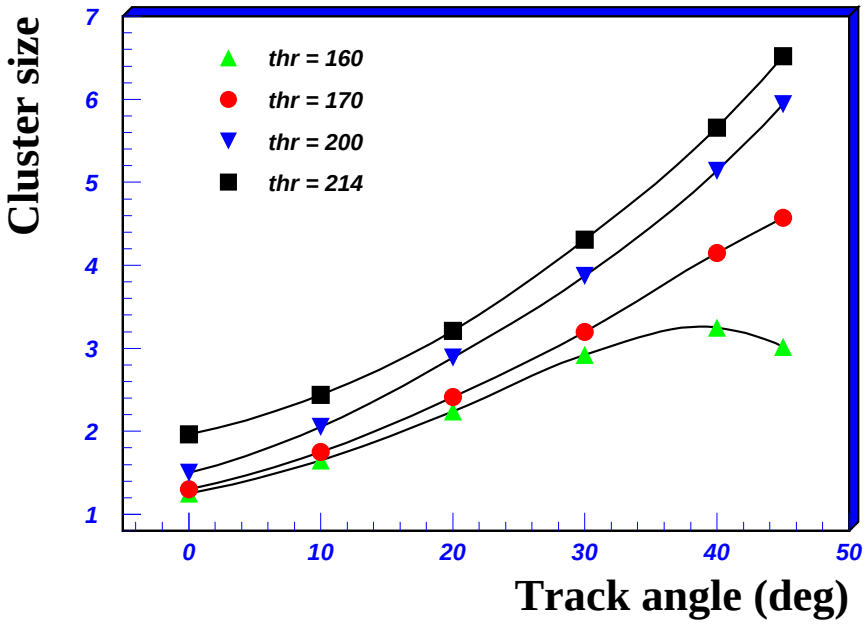

Figure 22: Average cluster size as a function of the track incidence angle for thresholds settings of 214, 200, 170 and 160 DAC units.

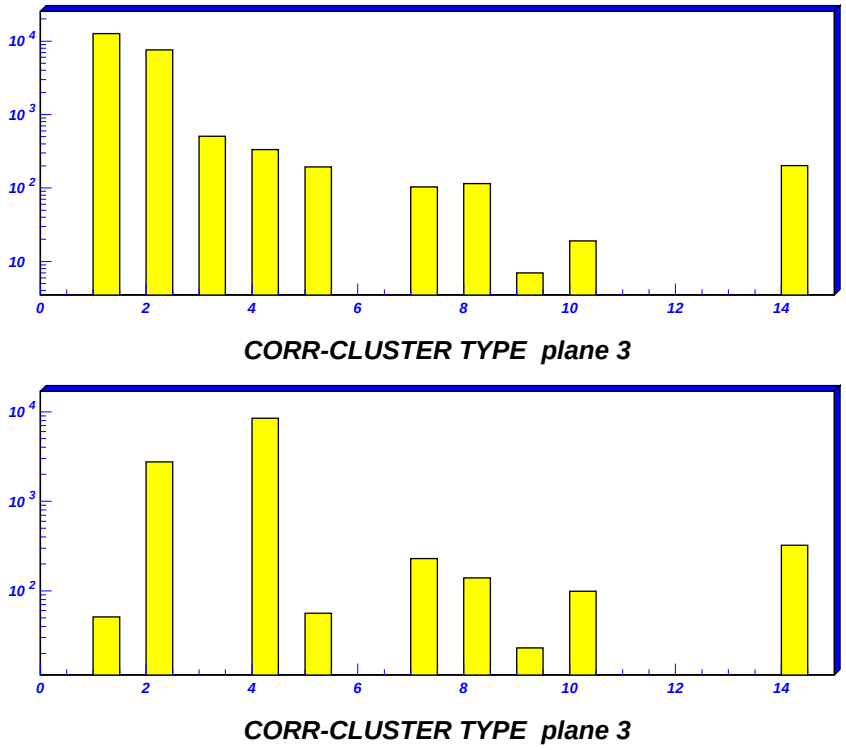

Figure 23: Cluster topology distributions for threshold settings of 200 DAC units, at 0 and 20 degrees incidence angles (top and bottom respectively).

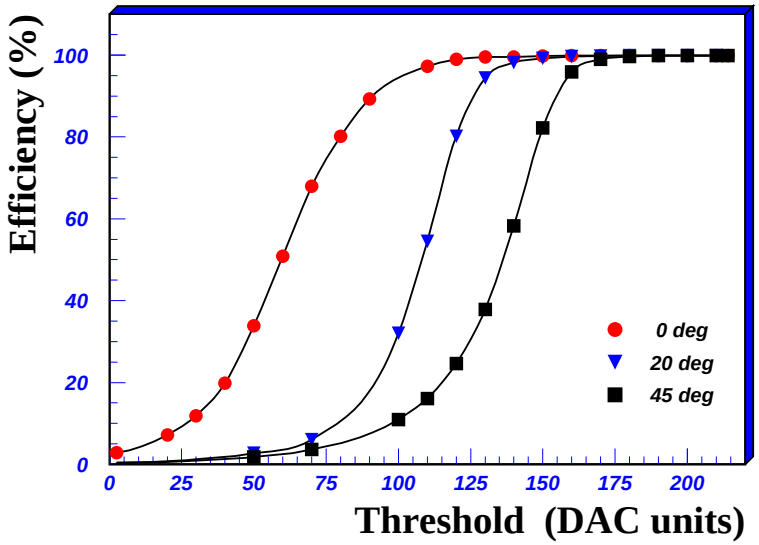

Figure 24: Detection efficiency as a function of the threshold for 0, 20 and 45 degrees track incidence angles.

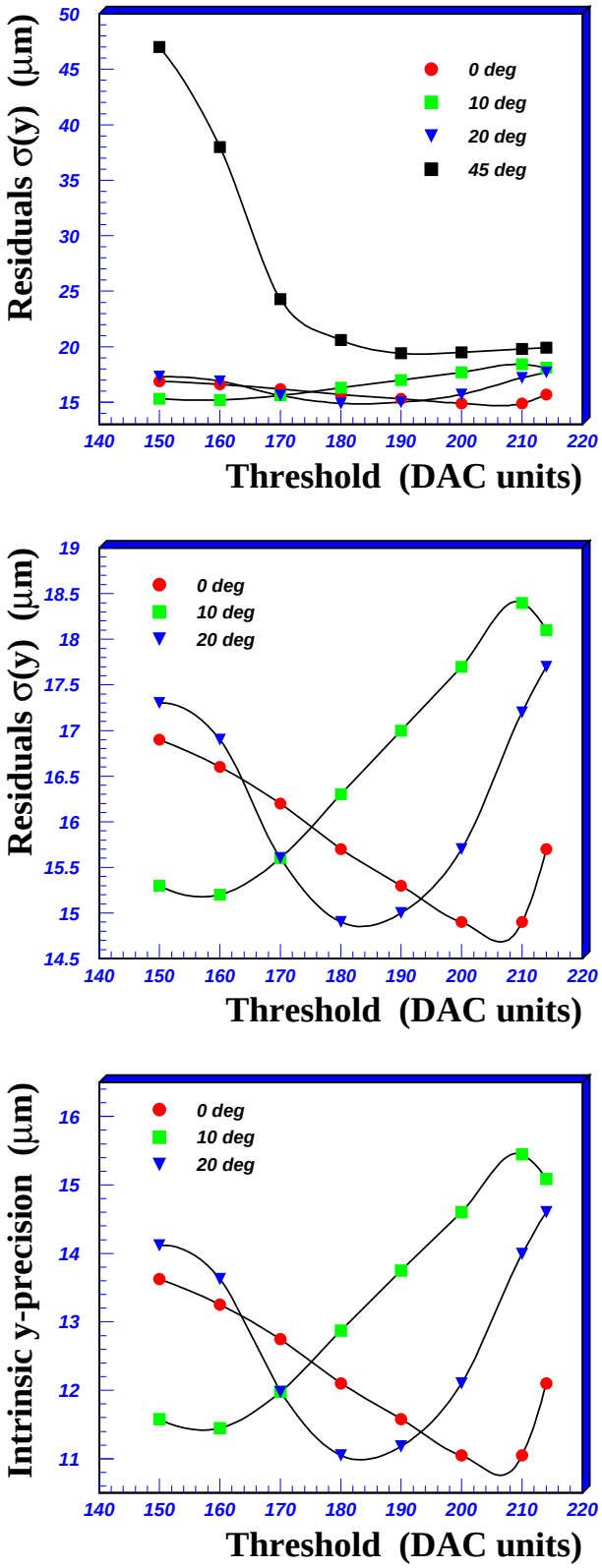

Figure 25: Widths of track residuals in the y coordinate at different track incidence angles (top and middle) and corresponding intrinsic precision (bottom) as a function of the threshold setting.

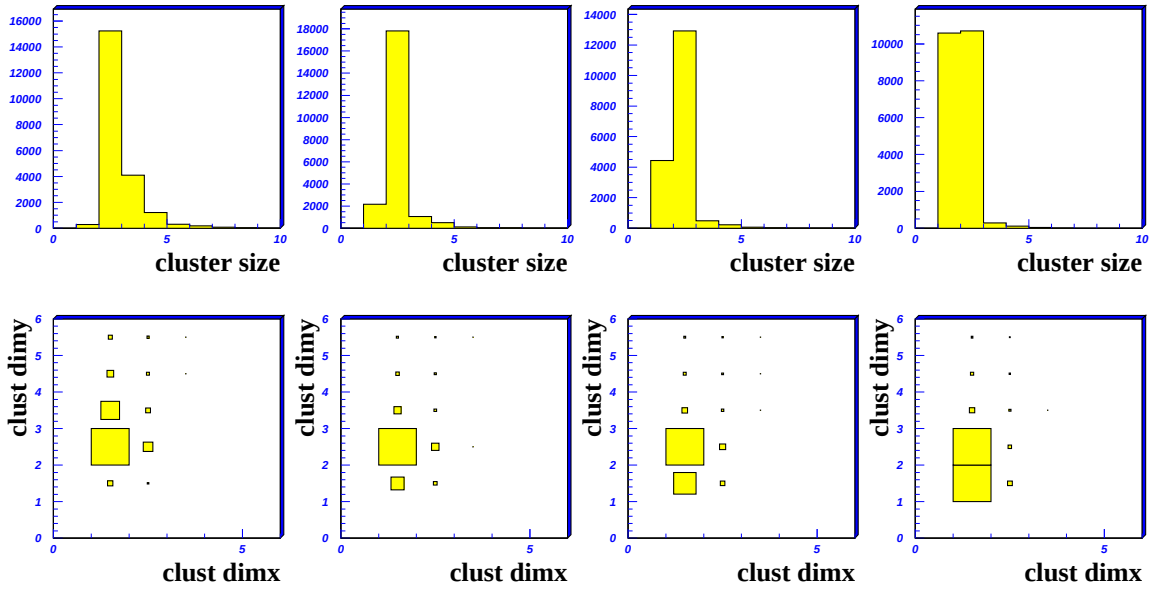

Figure 26: Cluster distributions for 10 degrees inclination angle tracks: from left to right threshold settings correspond to 214, 200, 180 and 150 DAC units.

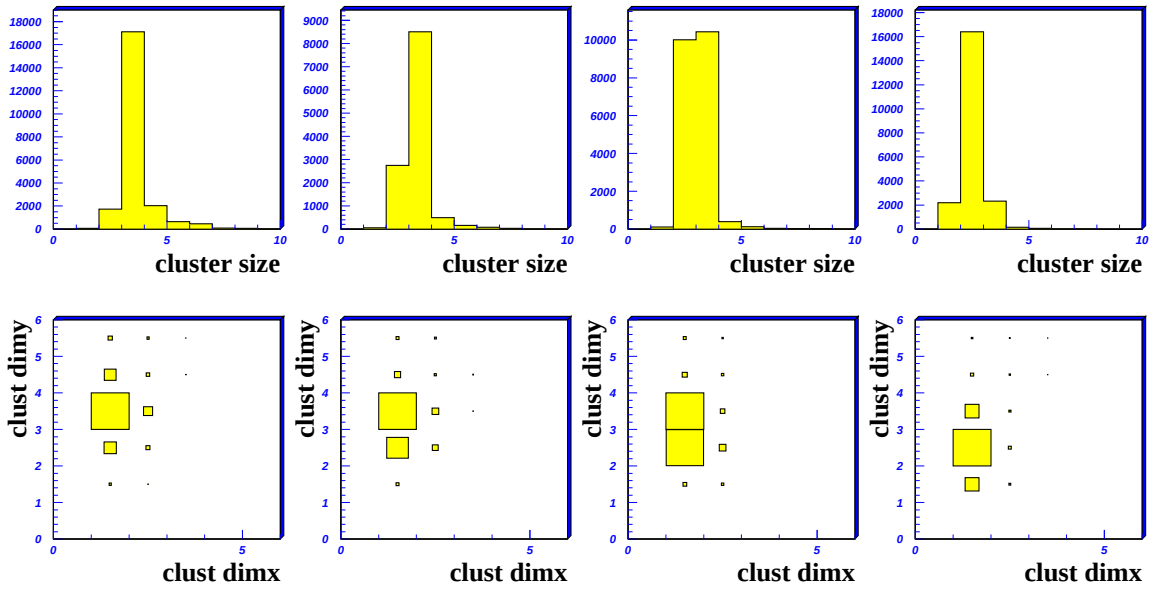

Figure 27: Cluster distributions for 20 degrees inclination angle tracks: from left to right threshold settings correspond to 214, 200, 180 and 150 DAC units.